



1 Gradients of Column CO₂ across North America from the 2 NOAA Global Greenhouse Gas Reference Network

3 Xin Lan^{1, 2}, Pieter Tans¹, Colm Sweeney^{1, 2}, Arlyn Andrews¹, Andrew Jacobson^{1, 2}, Molly
4 Crotwell^{1, 2}, Edward Dlugokencky¹, Jonathan Kofler^{1, 2}, Patricia Lang¹, Kirk Thoning¹, Sonja
5 Wolter^{1, 2}

6 ¹National Oceanic and Atmospheric Administration, Earth System Research Laboratory, Boulder, 80303,
7 Colorado, USA

8 ²University of Colorado, Cooperative Institute for Research in Environmental Sciences, Boulder, 80309, Colorado,
9 USA

10

11 *Correspondence to:* Xin.Lan (xin.lan@noaa.gov)

12 **Abstract.** This study analyzes seasonal and spatial patterns of column carbon dioxide (CO₂) over North
13 America calculated from aircraft and tall tower measurements from the NOAA Global Greenhouse Gas Reference
14 Network from 2004 to 2014. Consistent with expectations, gradients between the eight regions studied are larger
15 below 2 km than above 5 km. The 11-year mean CO₂ dry mole fraction (XCO₂) in the column below ~330 hPa (~ 8
16 km above sea level) from NOAA's CO₂ data assimilation model, CarbonTracker (CT2015), demonstrates good
17 agreement with those calculated from calibrated measurements on aircraft and towers. Total column XCO₂ was
18 attained by combining modeled CO₂ above 330 hPa from CT2015 with the measurements. We find large spatial
19 gradients of total column XCO₂ during June to August, and the north and northeast regions have ~3 ppm stronger
20 summer drawdown than the south and southwest regions. The spatial gradients of total column XCO₂ across North
21 America mainly reflect large-scale circulation patterns rather than regional surface sources and sinks. We have
22 conducted a CarbonTracker experiment to investigate the impact of Eurasian long-range transport. The result
23 suggests that the large summer time Eurasian boreal flux contributes about half of the north-south column XCO₂
24 gradient across North America. Our results confirm that continental-scale total column XCO₂ gradients simulated by
25 CarbonTracker are realistic and can be used to evaluate the credibility of spatial patterns from satellite retrievals,
26 such as the long term average spatial patterns from satellite retrievals reported for Europe which show larger spatial
27 difference (~ 6 ppm) and scattered hot spots.

28 1 Introduction

29 Atmospheric measurements of carbon dioxide (CO₂) from ground and airborne platforms have greatly increased our
30 knowledge of the global carbon cycle. Observations of CO₂, including the NOAA Global Greenhouse Gas
31 Reference Network (GGGRN), initially emphasized ground-based measurements. These observations, started by
32 C.D. Keeling, have monitored the CO₂ trend on both regional and global scales for over 50 years (e.g., Keeling and
33 Rakestraw, 1960; Tans et al., 1989). In addition, the frequency and spatial distribution of airborne measurements
34 have increased rapidly in the last two decades, providing important information about horizontal and vertical
35 variability of atmospheric CO₂ (e.g., Gerbig et al., 2003; Choi et al., 2008; Biraud et al., 2013). Routine aircraft



36 measurements from the NOAA/ESRL GGGRN monitor the large-scale distributions of a suite of trace gases,
37 including CO₂, under the influence of continental processes (Sweeney et al., 2015). A very successful approach has
38 been to employ commercial aircraft as a platform for CO₂ measurements, such as Japan's CONTRAIL
39 (Comprehensive Observation Network for TRace gases by AirLiner) project which has provided valuable
40 information for CO₂ in the high troposphere and lower stratosphere (Machida et al., 2002; Machida et al., 2008).
41 Vertical profiles of atmospheric CO₂ reflect the combined influences of surface fluxes and atmospheric mixing.
42 Vertical profiles are particularly useful for evaluating vertical mixing in atmospheric transport models that are used
43 for inverse modeling (e.g. Stephens et al., 2007) to derive estimates of regional- to continental-scale CO₂ sources
44 and sinks (e.g., Tans et al., 1990; Gurney et al., 2002; Gurney et al., 2004; Ciais et al., 2010;).

45 While CO₂ sources and sinks are better constrained at the global scale by global mass balance, it remains
46 challenging to accurately resolve CO₂ sources and sinks at regional-to continental-scale, the apportionment of which
47 depends on relatively minor variations of the observed spatial and temporal patterns of CO₂. When averaging over a
48 few months and longer the largest portion of the variations over continents results from hemispheric-scale terrestrial
49 uptake (photosynthesis)/emissions (respiration) and fossil fuel emissions, while regional net fluxes can make a
50 relatively small contribution to the signal. For example, a simple mass balance argument shows that all U.S. CO₂
51 emissions from fossil fuel burning (~1.4 Pg yr⁻¹) create a total column enhancement of only 0.6 ppm on average in
52 air parcels over the East Coast compared to the West Coast and Gulf Coast if we assume a residence time of the
53 emissions of 5 days to pass the contiguous U.S. (~8×10¹² m²).

54 With careful calibration, air handling, and analysis, the uncertainties of in-situ measurements are less than 0.1
55 ppm. However, in-situ observation networks are sparse in global and regional coverage. Remote sensing data
56 radically increase the number of observations and capture under-sampled regions. It is likely to have a valuable
57 impact on our understanding of the carbon cycle. However, both the precision and the potential of even very small
58 systematic biases in remote sensing measurements need to be carefully evaluated. Vertical profiles from in-situ CO₂
59 measurements have been used to evaluate ground-based total column XCO₂ (X stands for dry mole fraction)
60 determinations, such as those from the Total Carbon Column Observing Network (TCCON) (Washenfelder et al.,
61 2006; Wunch et al., 2010; Messerschmidt et al., 2011; Tanaka et al., 2012). The uncertainty of TCCON total column
62 CO₂ is reported to be 0.4 ppm (1σ) after comparison to aircraft measurements (Wunch et al., 2010). Vertical profiles
63 are also used to evaluate satellite retrievals of total column XCO₂, such as those from the Tropospheric Emission
64 Spectrometer (TES) (Kulawik et al., 2013) and the Greenhouse Gases Observing SATellite (GOSAT) (Inoue et al.,
65 2013, 2016; Saitoh et al., 2016). Satellite retrieval products have known and unknown biases (due to errors in
66 spectroscopy, viewing geometry, spatial differences in clouds and aerosols, surface albedo, etc.) that can result in
67 false horizontal gradients in total column XCO₂ for inverse estimates of sources (Miller et al., 2007; Crisp et al.,
68 2012; Feng et al., 2016). After correction for known biases, the GOSAT total column CO₂ retrievals biases range
69 between -2.09 to 3.37 ppm (mean = 0.11 ppm) across different aircraft sites over land, compared with aircraft-based
70 total column XCO₂ (Inoue et al., 2016). By comparing with TCCON, the Orbiting Carbon Observatory-2 (OCO-2)
71 retrieval of total column XCO₂ was estimated to have a mean difference less than 0.5 ppm with RMS differences
72 typically below 1.5 ppm after bias correction (Wunch et al., 2016). The overall uncertainty of satellite retrievals is



73 relatively large compared with the total column XCO₂ calculated from in-situ measurements. Total column XCO₂
74 calculated from vertical profiles from the Japanese CONTRAIL project (Machida et al., 2008) and from the NOAA
75 Carbon Cycle and Greenhouse Gas aircraft program (Sweeney et al., 2015) complemented with simulated profiles
76 from a chemistry–transport model above the maximum altitude of the data have uncertainty less than 1 ppm
77 (Miyamoto et al., 2013). The relatively small uncertainty of the in situ-based total column XCO₂ suggests that they
78 can be used to evaluate satellite retrievals of column averaged CO₂. Since aircraft profiles co-located with satellite
79 retrievals are rare, it is useful to consider the statistics of total column XCO₂ fields derived from repeated aircraft
80 profiles over particular locations.

81 The effect of satellite column averaging kernels and a priori profiles when comparing aircraft-based column
82 XCO₂ with GOSAT retrievals has been assessed by Inoue et al. (2013). For the case considered, application of the
83 averaging kernel and a priori profile to simulate total column XCO₂ was generally within ± 0.1 ppm of the density
84 weighted total column, suggesting that the averaging kernels can only account for small part of the overall
85 uncertainty of the GOSAT total column XCO₂ (Inoue et al., 2013).

86 Transparent and objective estimates of CO₂ sources and sinks derived from atmospheric measurements are
87 paramount for validating emissions reduction efforts and other mitigation policies, and for lowering the uncertainties
88 of carbon cycle-climate feedbacks. The latter are major ambiguities in predicting future climate, such as potential
89 uncontrolled CH₄ and CO₂ emissions from warming permafrost in Arctic regions. Satellite retrievals of total column
90 XCO₂ can significantly improve estimates of source and sinks only if they are sufficiently precise and accurate
91 (Rayner and O'Brien, 2001; Houweling et al., 2004), meaning that even very small systematic errors (biases) must
92 be eliminated. Here, we analyze the spatial and temporal variability of column CO₂ over North America using well-
93 calibrated CO₂ measurements from aircraft and tall tower, and we use model results from NOAA's CarbonTracker,
94 version CT2015 (Peters et al. 2007, with updates documented at <http://carbontracker.noaa.gov>) to investigate the
95 primary drivers of variability in total column XCO₂. The aircraft data enable direct analysis of column CO₂
96 characteristics, which is the fundamental step for accurate apportionment of sources and sinks. This study focuses on
97 the long-term averaged column CO₂ gradient and the contributions of different vertical layers to the total column
98 variability. It can serve as a reference for evaluating current and future column CO₂ retrievals from both ground and
99 satellite platforms.

100 **2 Methods**

101 **2.1 Aircraft and tall tower sampling**

102 Aircraft sampling in the NOAA GGGRN intends to provide vertical profiles of long-lived trace gases to capture
103 their seasonal and interannual variability. The aircraft sampling system consists of 12 borosilicate glass flasks in
104 each programmable flask package (PFP), a stainless-steel gas manifold system, and a data logging and control.
105 These flasks (0.7 L each) are pressurized to obtain 2.2 L of sample air from each target altitude. Air samples are then
106 shipped back to NOAA/ESRL for carefully calibrated and quality-controlled measurements. Carbon dioxide is
107 measured using a nondispersive infrared analyzer. Long-term measurements at ~15 sites are carried out using light



108 aircraft that can reach 8.5 km. Air samples are collected mostly during late morning to early afternoon, when the air
109 mass within the planetary boundary layer (PBL) is generally well mixed, and CO₂ enhancement near the ground
110 from plant respiration during the night has been mixed throughout the boundary layer. Normally, the aircraft follows
111 a pre-decided route such that most samples are collected within 0.1° of the site location. The sampling frequency
112 varies from site to site, currently from twice a month to once every 1.5 months. For more sampling details, quality
113 control discussions, and an evaluation of the sampling frequency, please refer to Sweeney et al. (2015). More
114 information on the aircraft sites can be found at <http://www.esrl.noaa.gov/gmd/ccgg/aircraft/>. We estimate the
115 uncertainty of individual measurements of CO₂ in flask air (68% confidence level) at 0.08 ppm. However, we have
116 seen evidence of positive biases for samples collected using older flasks that may contain contaminants. Andrews
117 et al. (2014) reported biases that increased from <0.1 ppm in 2008 to an average offset in 2013 of 0.36 ppm. The
118 aircraft sampling protocol was modified starting in August 2014 to mitigate this bias. For samples collected prior the
119 protocol change, laboratory tests showed that new/clean flasks have zero bias, but some older/dirty flasks could have
120 biases of > 1 ppm. This bias is not consistent among individual flasks and increasing over time (Andrews et al.,
121 2014), the potential bias is hard to quantify for measurements before August 2014. Thus, the high bias is not
122 corrected in our study. More recently, low bias has been found in PFP measurements when the ambient humidity is
123 high, based on comparisons of PFP measurements with data from in-situ analyzers at tall towers. We are working to
124 understand and quantify this bias, and for this study we have derived a preliminary correction factor, which shows a
125 linear trend with -1.4 ppm CO₂ offset per 1% above 1.7% of ambient water content (in mole fractions). Only ~ 4%
126 of total aircraft measurements or ~ 12% of those below 2 km are impacted by humidity higher than 1.7%, for which
127 we have applied corrections before data analysis. The mean correction applied is 0.53 ± 0.4 (1 σ) ppm for the
128 impacted data.

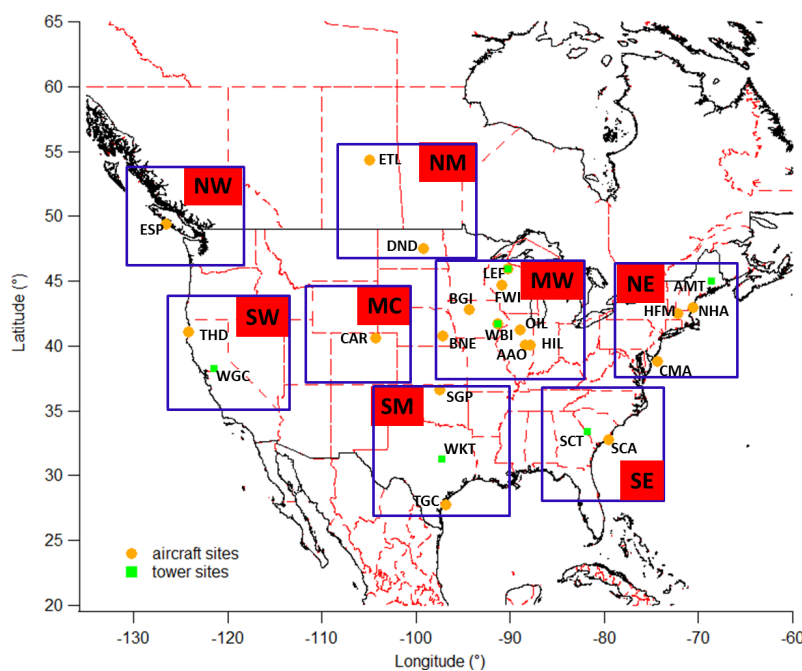
129 The NOAA tall tower network measures CO₂ and other trace gases within the continental boundary layer.
130 Continuous in-situ measurements are conducted using nondispersive infrared (NDIR) absorption sensors and cavity
131 ring-down analyzers. The long-term stability of these systems is typically better than 0.1 ppm for CO₂ (Andrews et
132 al., 2014). Most tall tower sites have more than one air intake height. In this study, continuous in-situ measurements
133 from the highest intake are used to minimize potential influences from local sources. More information concerning
134 the tower sites can be found at <http://www.esrl.noaa.gov/gmd/ccgg/insitu/>. For the column XCO₂ calculation, tower
135 data only from 10:00-17:00 local standard time (LST) on flight days are averaged to one data point per day, as a
136 complement to vertical profiles within the PBL.

137 2.2 Site description

138 We analyze data from 19 aircraft sites and 6 tall tower sites during 2004 to 2014 (see Table S1 for a summary of site
139 conditions). After considering the geographic distribution of these sites in North America, we group them into eight
140 regions for spatial comparisons (Fig. 1). The northern west (NW) and southern west (SW) regions represent the
141 inflow area in the west coast of US, directly downwind of the Pacific Ocean at both higher elevations. The northern
142 mid-continent (NM) region represents the boreal forest and agriculture region in north-central North America. The
143 mid-continent (MC) region represents a dry landscape due to its high elevation (above 1.5 km on average) and semi-



144 arid climate. The mid-west (MW) region is strongly influenced by agriculture and temperate forest. The southern
145 mid-continent (SM) represents the south-central humid temperate region, with inflow from the Gulf of Mexico
146 during summer. The northeast (NE) region represents the temperate forest in north-east coast of U.S., which is
147 mostly downwind of regions to the west above the PBL, and downwind of its south-west regions within the PBL.
148 The southeast (SE) region represents the warm temperate region in the south-east coast of U.S.
149



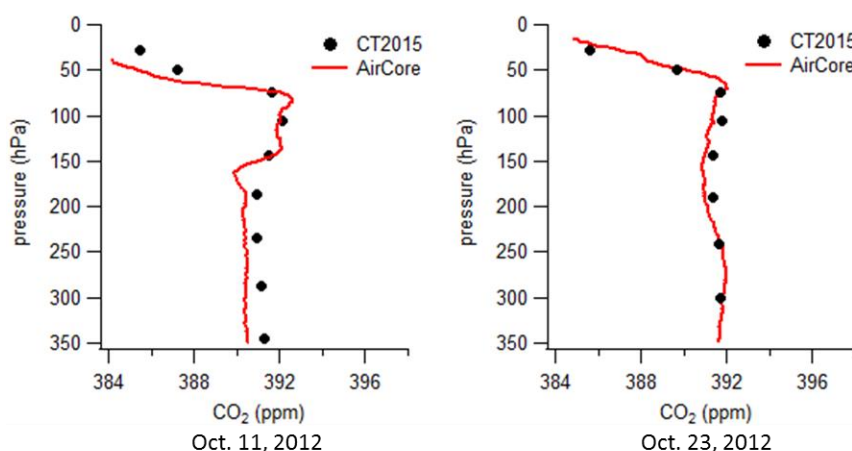
150
151 **Fig. 1.** Aircraft, tall tower, and high elevation/tower sites in the NOAA GGRN. The eight boxes define regions
152 that are further discussed for spatial pattern comparison.

153 2.3 Smoothing of the reference data and column XCO₂ calculation

154 We use Mauna Loa Observatory (MLO) as a reference site. Long-term trend of CO₂ measurements from this site is
155 removed before combining multiple years of data to calculate long-term averages. MLO is located at 19.536°N,
156 155.576°W, and 3397 m above sea level. Carbon dioxide measurements from this site are widely used to represent
157 background CO₂ in the Northern Hemisphere. For our study, a function consisting of a quadratic polynomial and
158 four harmonics is fitted to the MLO data, adopted from the method described by Thoning et al. (1989). Residuals of
159 the data from this function are smoothed by a low-pass filter with full-width at half-maximum in the time domain of
160 1.1 years. The smoothed residuals are then added back to the polynomial part of the function to produce the long-
161 term deseasonalized trend. This trend (see Fig. 2) is subtracted from all aircraft and tall tower measurements, as well
162 as from CarbonTracker model results (CarbonTracker - MLO deseasonalized trend, CarbonTracker results presented
163 in this study are the differences relative to observed MLO deseasonalized trend). We use ‘Δ’ to represent detrended



164 data in the following text and figures. The choice of reference site is not important for this study, since we focus on
165 examining the relative seasonal patterns of the detrended spatial and vertical distributions of CO₂ instead of the total
166 changes in CO₂ abundance attributed to global surface fluxes.
167



168
169 **Fig. 2.** Carbon Tracker (CT2015) simulations compared with AirCore in-situ measurements in upper atmosphere.
170 AirCore profiles in the left and right panels are sampled near CAR and SGP, respectively.
171

172 We calculate partial column average CO₂ dry mole fraction using tall tower and aircraft data, and the total
173 column by adding simulations of high altitude CO₂ (above 330 hPa, ~ 8 km above sea level) from CarbonTracker.
174 Since geometric height from the onboard Global Positioning System (GPS) (after 2006) or inferred from the aircraft
175 altimeter or pressure altitude is archived with each aircraft measurement, we first convert geometric height (in
176 meter) to pressure (in hPa) for the pressure-weighted column XCO₂ calculation. This conversion uses geopotential
177 data from NOAA/NCEP North American Regional Reanalysis (NARR) (Mesinger et. al, 2004), available at
178 <https://www.esrl.noaa.gov/psd/data/gridded/data.narr.html>, in which the geopotential is a function of latitude,
179 longitude, pressure altitude and time. We interpolate the geopotential field vertically to retrieve pressure, and then
180 calculate dry pressure by incorporating specific humidity data from NARR. Eventually we use a trapezoidal method
181 to integrate over detrended vertical profiles for dry-pressure-weighted column average. For the long-term averaged
182 column ΔXCO_2 calculation, a long-term mean vertical profile is first constructed for each month by combining 11-
183 year detrended data together and then average data in each 40 hPa vertical bin. To look at the long-term averaged
184 total column ΔXCO_2 from individual aircraft sites, we combine aircraft data with upper-layer CT2015 simulations.

185 The NOAA CarbonTracker model assimilates CO₂ measurements from surface sampling networks and tall
186 towers to generate global 3D fields of atmospheric CO₂ mole fraction. The Carbon Tracker model has evolved
187 significantly since Peters et al. (2007). A detailed description of this model is provided in documents available at
188 <http://carbontracker.noaa.gov>. Our study utilizes CarbonTracker results from the 2015 release (CT2015), publicly
189 accessible at <ftp://aftp.cmdl.noaa.gov/products/carbontracker/co2/CT2015/molefractions/>. This version provides

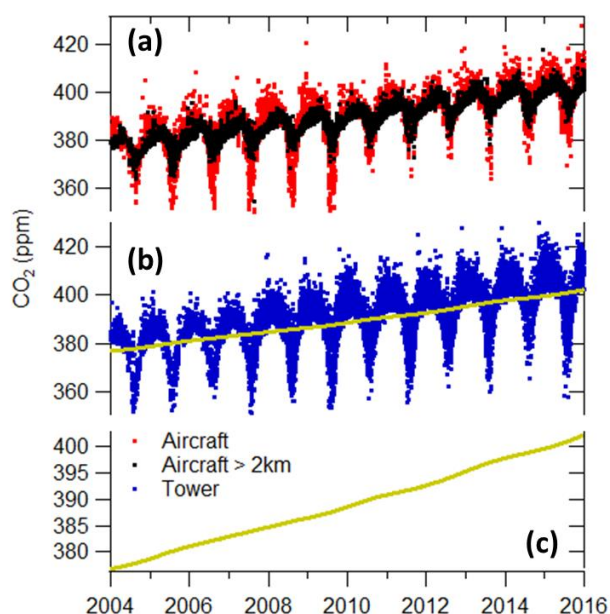


190 CO₂ mole fraction over North America with 1° × 1° spatial and 3 hour temporal resolutions, which are analyzed in
191 Sect. 3.2 and 3.3. Total column CO₂ calculated from CT2015 global data with 3° × 2° spatial resolution is also
192 presented in the supporting information (SI). We have evaluated the performance of CarbonTracker in upper
193 atmosphere (330 to 0 hPa) by comparing its simulations with in-situ measurements from 9 AirCore profiles (Karon
194 et al., 2010) sampled in 2012-2014. AirCore is a ~150 m stainless steel tube that utilizes changes in ambient
195 pressure for passive sampling of the vertical profile. It is released using balloons and it collects a continuous sample
196 as it descends. It is then measured by an analyzer after it is recovered. More information about AirCore system can
197 also be found at <https://www.esrl.noaa.gov/gmd/ccgg/aircore/>. Figure 2 shows examples of AirCore profiles
198 compared with CT2015 in the upper atmosphere, which demonstrates good agreement. We also compare partial
199 column (330 to 0 hPa) averages from the 9 AirCore profiles and CT2015. Results from CT2015 agree generally well
200 with AirCore, with difference ranging from 0.03 to 1.22 ppm (mean value equals 0.66 ppm), which suggests that
201 CT2015 may have a high bias that can contribute to 0.66×1/3=0.22 ppm overestimate on average to the total column
202 average. However, AirCore is in the process of rigorous evaluation, the differences between AirCore and CT2015
203 are not well characterized yet since we only have a limited amount of AirCore data. It is unclear whether the
204 potential bias of CT2015 in this partial column is dependent on time or sampling location. Adding a constant bias
205 correction to all regions will not change the spatial gradients that we focus on in this study. Thus no correction is
206 applied when using CT2015 simulations to represent the upper 1/3 of the total column.
207 For uncertainty estimates, we use a ‘bootstrap’ method that uses random resampling and repetition of individual
208 vertical profiles (low bias due to high humidity was corrected), with 100 Monte Carlo runs for each column average
209 calculation. Uncertainty is then defined as one standard deviation of the 100 Monte Carlo results.

210 **3 Results and Discussions**

211 **3.1 Seasonal patterns and spatial gradients**

212 Typically one aircraft profile contains measurements at 12 different altitudes. Column ΔXCO_2 can be computed for
213 each profile using the method described in Sect. 2.3 (Fig. S1). Figure 3 shows aircraft (at all altitudes) and tower
214 data (daily averages for 10:00-17:00 LST data) from all sites used in this study. Aircraft data above 2 km exhibit
215 much smaller seasonal variations than the full dataset, because the variations are mainly driven by CO₂ sources and
216 sinks near Earth’s surface. CO₂ concentration is enhanced in the shallow wintertime PBL primarily due to reduced
217 plant photosynthesis and ecosystem respiration combined with slightly increased fossil fuel emissions. During
218 summer the PBL is deeper, and depletions within the PBL are due to strong terrestrial uptake that dominates over
219 emissions especially during June through August. During summer of 2010 to 2012, CO₂ from aircraft measurements
220 appears higher than other years in Fig.3; however, similar characteristics are not present in tower data. This
221 difference is due to a decrease in sampling frequency at several aircraft sites that resulted in an aliased picture of the
222 full summer drawdown. Since we focus on climatological mean of 11 years of data in our study, this influence is
223 eliminated by combining 11 years of data together into one “average year”.



224
225 **Fig. 3.** CO₂ observations from aircraft (a) and towers (b). The yellow line in (b) illustrates the deseasonalized trend
226 at Mauna Loa (MLO), same as in (c), in which y-axis expanded.

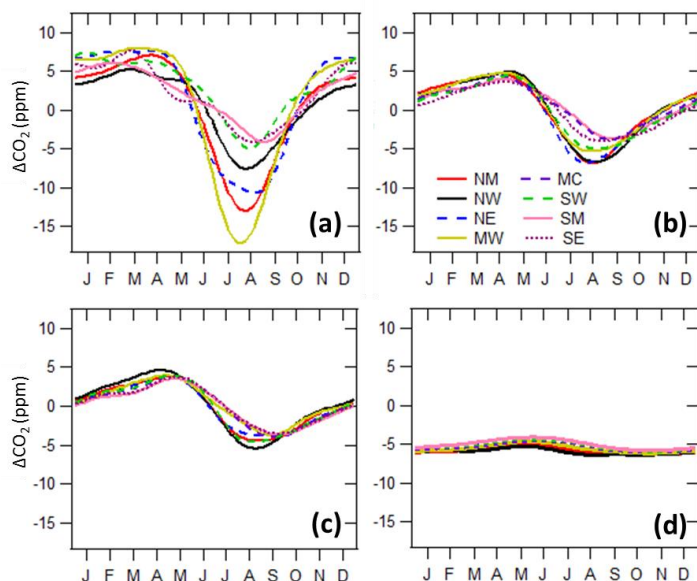
227
228 To investigate the contributions of different altitudes to spatial gradients between regions, we divided all
229 measurement data into three layers according to their sampling altitudes: below 2 km, 2 - 5km, and 5 - 8.5 km masl
230 (Fig. 4). Smooth seasonal curves are attained from fitting data with four harmonics using the method described by
231 Thoning et al. (1989). The peak-to-valley amplitudes of the seasonal cycles below 2 km are the largest among the
232 three layers for most regions, with a minimum of 10.3 ppm in SM and a maximum of 25.0 ppm in MW. The
233 seasonal variation amplitudes decrease to 7.7-11.5 ppm in the 2 - 5 km layer, and further decrease to 7.2-10.0 ppm in
234 the 5 - 8.5 km layer. We also observe that the seasonal cycle drawdown occurs later in the layers above 2 km (see
235 Fig. S2, which provides similar information as Fig. 4, but seasonal curves from different vertical layers are grouped
236 by regions to facilitate comparisons of the phases of seasonal cycles). The seasonal CO₂ drawdown below 2 km is
237 mainly influenced by terrestrial photosynthesis and gradients are influenced by local to regional fluxes, with an
238 earlier onset of drawdown in southern regions than in northern regions. The seasonal cycle aloft is damped and
239 lagged compared to the PBL, with influences from throughout the Northern Hemisphere and with spatial gradients
240 likely driven by large-scale transport. The NW, SW, SM, and SE inflow regions have significant delays of more
241 than one month in the 2 - 5 km layer compared with the surface layer, which is likely due to the delayed phase of the
242 seasonal cycle in well-mixed air coming from the oceans. Vertical homogeneity of air over ocean was observed
243 during the HIAPER Pole-to-Pole Observations (HIPPO) aircraft campaign (Wofsy et al., 2011; Frankenberg et al.,



244 2016). As air masses are transported further inland, we observe reduced discrepancies of the timing of CO₂
245 drawdown between surface and upper layer air (2-5 km), which may be associated with the increased influence of
246 the land surface in the mid-troposphere due to strong convection over land. CO₂ drawdown in the 5 - 8.5 km layers
247 also occurs later than in the 2 - 5 km layers in most regions; however, differences between these two layers are
248 small. The declining amplitude and delayed phase of the seasonal cycle with altitude have been noted often (e.g.,
249 Tanaka et al., 1983; Ramonet et al., 2002; Gerbig et al., 2003, Sweeney et al. 2015). It demonstrates that there is lot
250 of important information in the vertical profile that is diminished in observations of the total column.

251 We find that the largest horizontal spatial gradients between regions occur below 2 km during summer time
252 (Fig. 4), with a maximum difference of ~15.5 ppm between MW and SM. SM and SW exhibit less pronounced
253 seasonal cycles, which is likely associated with air masses from the Gulf of Mexico and the Pacific Ocean,
254 respectively, whereas MW exhibits a deep summer drawdown partially as a result of strong regional forest and crop
255 uptake. Crevoisier et al. (2010) estimated the surface flux over North America using vertical CO₂ measurements and
256 average wind vectors, and reported that annually averaged land carbon flux at the western (including SW region)
257 and southern regions (including SM region) were neutral. The SE region also demonstrates a less pronounced
258 seasonal cycle with weaker summer drawdown compared with other northern regions, which may due to the sea-
259 breeze influence in summer within PBL. In wintertime, CO₂ levels in NE and MW are higher than in other regions,
260 which result from regional fossil fuel and terrestrial biogenic emissions combined with transport from the west and
261 south.

262 Higher altitude data (above 2 km) exhibit only small spatial gradients. In the 2 - 5 km layer, the largest gradient
263 is 4 ppm in summer (Fig. 4b). It further decreases to less than 3 ppm in the 5 - 8.5 km layer (Fig. 4c). Figure 4d
264 shows modeled CO₂ mole fractions from CT2015 for the upper troposphere and above (330 hPa to 0 hPa), which are
265 used to fill in above the aircraft profiles for calculation of total column ΔXCO₂. Spatial gradients in this layer are
266 less than 0.5 ppm, suggesting that the top third of the total column has little contribution to the spatial gradients of
267 the total column.



268

269 **Fig. 4.** Multi-year (2004-2014) average smooth seasonal curves of CO₂ relative to the long-term de-seasonalized
270 trend at Mauna Loa for different vertical layers: (a). Aircraft and tower data under 2 km, MC is not presented
271 because only limited data were available due to high surface elevations (>1.5 km on average) in this region; (b).
272 Aircraft data from 2 - 5 km; (c). Aircraft data from 5 - 8.5 km; (d). CT2015 model results for layers above 330 hPa
273 (~8.5 km) to 0 hPa (~80 km).

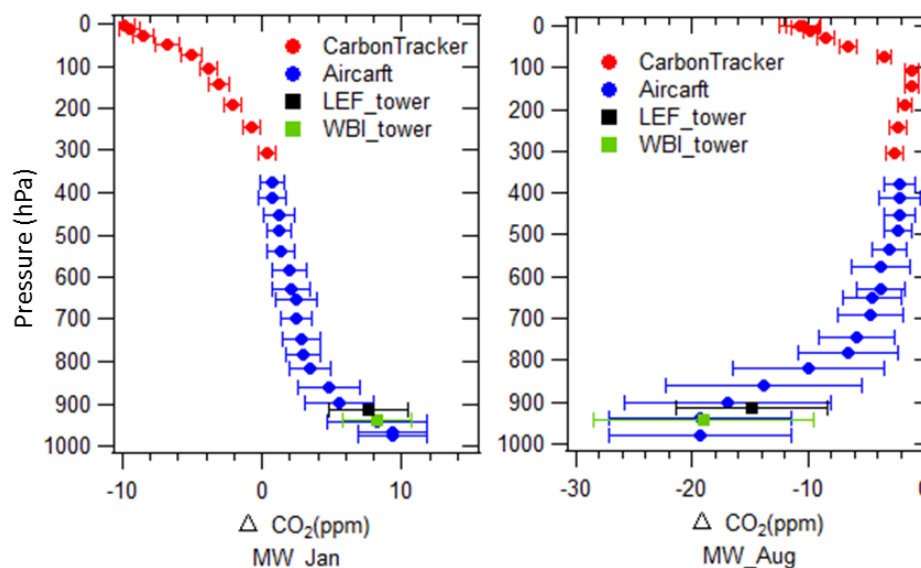
274 3.2 Long-term mean vertical profiles

275 To investigate the mean spatial gradients, we first calculate the long-term mean monthly vertical profiles as
276 described in Sect. 2.3. In addition, each tower serves as one additional layer in the mean profile. The long-term
277 mean tower data generally fit well in the vertical profiles from measurements of aircraft samples (Fig. 5 and Fig. 6),
278 suggesting that the biases described in Sect. 2.1 above do not significantly affect the long-term mean. To attain
279 profiles of the entire atmospheric column, upper layers (330 to 0 hPa) are filled in by CT2015, and the lowest data
280 point of the measured profile is extended to ground level, defined by the mean surface elevation in that region.

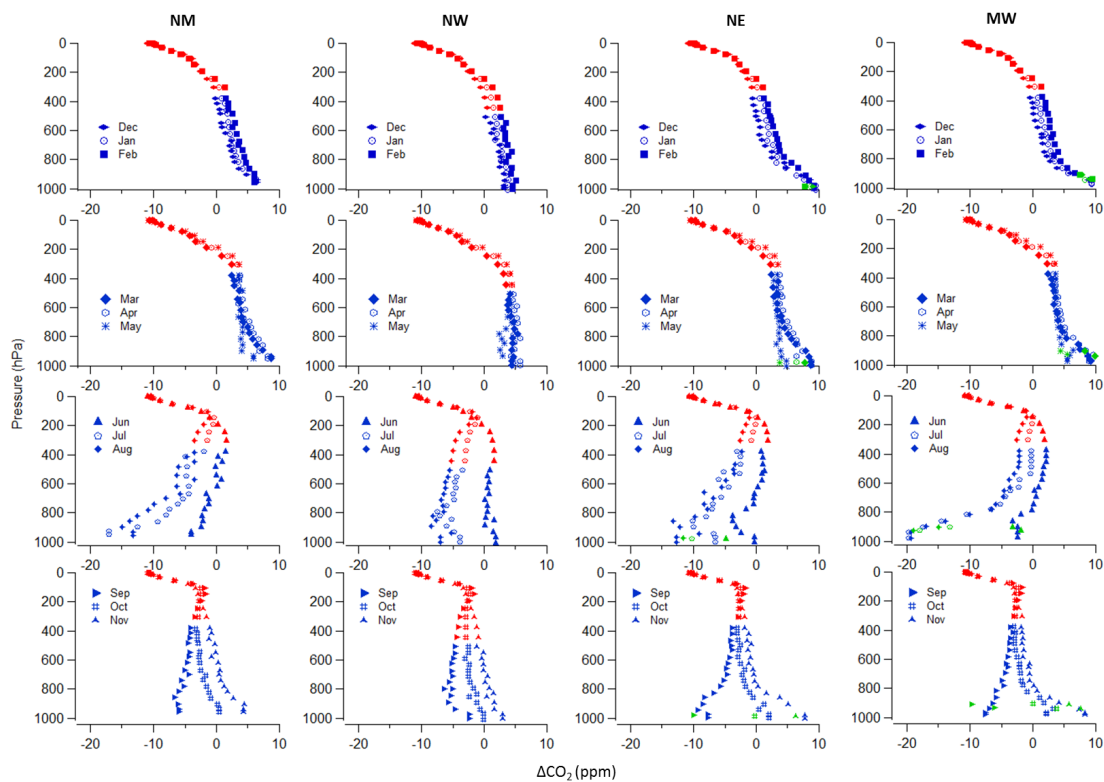
281 Figure 5 presents two examples of long term mean profiles with data variability, which is the one standard
282 deviation for each 40 hPa bin of aircraft data or for all flight-day tower data. Variability as large as 20 ppm is seen
283 within the PBL in the MW region in summer, which is due to strong and heterogeneous surface vegetation uptake
284 and ecosystem respiration combined with day-to-day changes in wind direction. All long-term mean monthly
285 vertical profiles are presented in Fig. 6, which shows the mean temporal and vertical variability of CO₂ in each
286 season, and further demonstrates the vertical propagation of seasonal CO₂ due to changes of surface flux. In
287 wintertime, monotonic decrease of CO₂ with altitude can be observed from all regions, in which high PBL CO₂ is
288 mainly driven by surface emissions and reduced vertical mixing (Denning et al., 1998; Stephens et al., 2007).



289 Surface CO₂ decreases dramatically in the growing season in those regions influenced by high plant activity, such as
290 NM and MW regions. For the summer vertical profiles in NE and SE region (east coast of the U.S.), the CO₂ mixing
291 ratio is elevated in the layer under 900 hPa followed by significant decreases in upper layers until 750 hPa, and then
292 increases with altitude until tropopause (Fig. 6). This is likely a feature of sea breeze influence. Lower-troposphere
293 air from the sea, lacking terrestrial uptake of CO₂, typically has higher CO₂ in summer compared with inland air.
294 Polluted air previously advected offshore can be brought back along with sea breeze. Without significant vertical
295 mixing over the marine surface, high levels of pollutants remain in those air masses. The convergence of sea breeze
296 with prevailing wind moving offshore may create a period with a stalled frontal structure that can aggregate air
297 pollutants (Banta et al., 2005). The convective internal boundary layer structure of the sea breeze system can
298 significantly reduce mixing height (Miller et al., 2003), and also induces higher CO₂ levels. When the sea breeze is
299 not dominant, air advected from southwest and west (the land) can also bring in polluted air with high CO₂ since this
300 region is downwind of continental U.S. emissions (Miller et al., 2012).

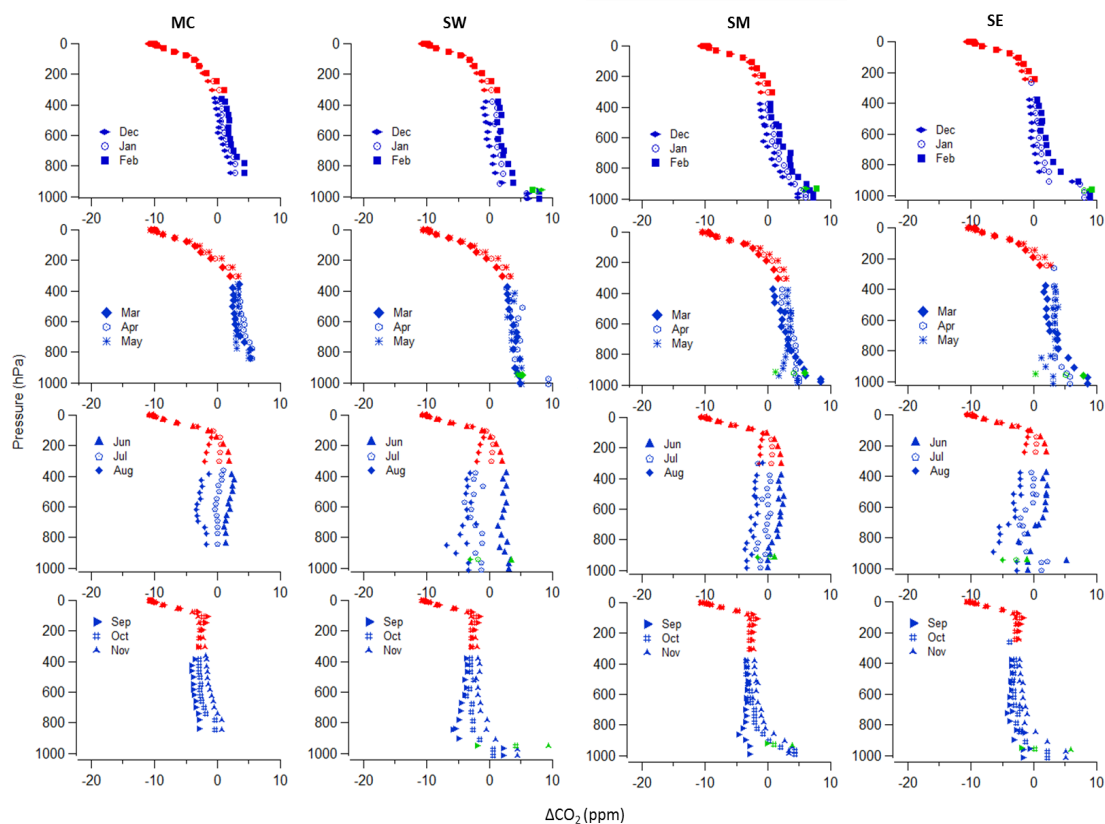


301
302 **Fig. 5.** Long-term mean (2004-2014) average vertical profiles in January (left panel) and August (right panel) in
303 region MW. Error bar shows one standard deviation.



304

305 **Fig. 6a.** Long-term mean (2004-2014) monthly vertical profiles in NM, NW, NE, MW (by column, from left to
306 right). Blue points were calculated from observations, red points were calculated from CT2015, and green points
307 were calculated from tower data.



308

309 **Fig. 6b.** Long-term mean (2004-2014) monthly vertical profiles in MC, SW, SM, SE (by column, from left to right).

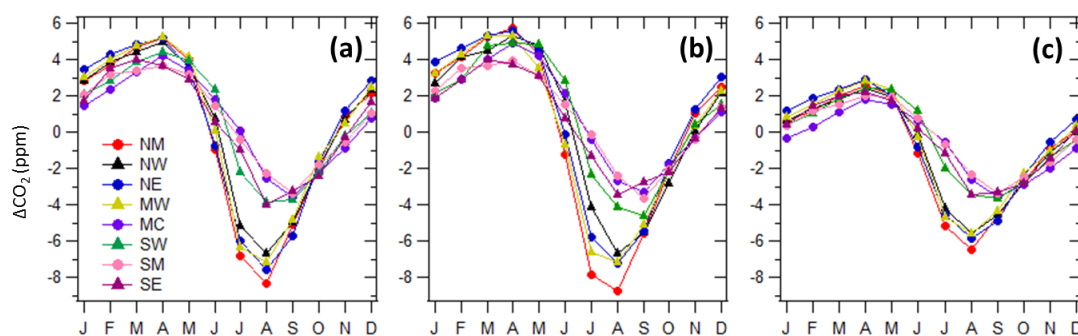
310 Blue points were calculated from observations, red points were calculated from CT2015, and green points were
311 calculated from tower data.

312



313 3.3 Partial column ΔXCO_2 and total column ΔXCO_2

314 Seasonal variations of monthly averaged partial column ΔXCO_2 demonstrate maximum values in April and
315 minimum values in August or September (Fig. 7a). The largest amplitude appears in NM, with peak-to-valley
316 difference up to 13.5 ppm. SW, SM, SE, and MC have similar amplitudes of 7-8 ppm, smaller than other regions. To
317 evaluate the performance of CT2015 on column ΔXCO_2 , CT2015 results are sampled to match the latitude,
318 longitude, altitude and time of actual measurements. Note that aircraft profiles are not assimilated in CT2015, so
319 aircraft data are independent of the CT2015 data assimilation. Figure 7b shows monthly partial columns of ΔXCO_2
320 calculated from CT2015, which demonstrate good agreement with results from measurements. Only small seasonal
321 biases exist in CT2015, with high bias occurring mostly in spring and early summer and low bias in September and
322 October (Fig. S3). The overall differences of monthly partial column ΔXCO_2 (CT2015 - measurements) mainly fall
323 in the range of -0.64 ppm (5th percentile) to 0.84 ppm (95th percentile) with a mean difference of 0.13 ppm. These
324 differences are of similar magnitude to the uncertainties of partial column ΔXCO_2 calculated from the measurements
325 (Fig. S4). It is clear that CT2015 captures the long-term mean variations of both phase and amplitude of partial
326 column XCO_2 reasonably well.
327



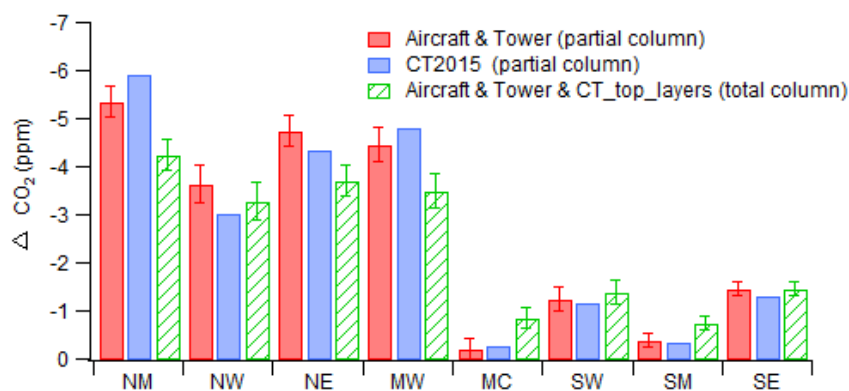
328
329 **Fig. 7.** (a). Partial column ΔXCO_2 calculated from aircraft and tower data; (b). Partial column ΔXCO_2 calculated
330 from CT2015; (c). Total column ΔXCO_2 calculated from aircraft and tower data and including the top layer data
331 from CT2015.

332

333 Total column ΔXCO_2 is presented in Fig. 7c. In regions NW, NM, NE, and MW, seasonal variations of total
334 column ΔXCO_2 are very similar in both phase and amplitude (8-9 ppm peak to valley). For SW, SM, SE, and MC,
335 amplitudes are ~5.5 ppm. The smallest spatial gradients occur during May and October, which result in maximum
336 differences among all regions of only 0.9 and 0.7 ppm, respectively. The largest spatial gradients occur during June,
337 July and August, which result in maximum differences of 2.4, 4.5, and 4.1 ppm, respectively. It is interesting that the
338 deepest drawdown is seen in region NM, not in region MW that encompasses the very intensive agricultural
339 activities in the U.S. mid-west, which suggest the possibility of strong upwind influence in the NM region. The



340 summer drawdown of total column ΔXCO_2 , represented by the June to August average from CT2015, has a
341 magnitude that is similar to observations with differences no more than 1 ppm (Fig. 8). Based on the seasonal
342 patterns of total column ΔXCO_2 and strength of summer drawdown, we can separate the eight regions into two
343 groups. The group with NW, NM, NE, and MW, has ~ 3 ppm stronger drawdown than the group with SW, SM, SE,
344 and MC. For winter total column ΔXCO_2 (December to February average), the maximum spatial difference is only
345 1.6 ppm, with the highest total column ΔXCO_2 of 1.2 ppm in NE and the lowest value of -0.3 ppm in MC.
346



347
348 **Fig. 8.** Long-term mean (2004-2014) June to August partial and total column ΔXCO_2 . Error bars represent one
349 standard deviation from the bootstrap uncertainty calculation (see Sect. 2.3).
350

351 3.4 Influence of large scale circulation

352 Figure 9 shows long-term mean summer column ΔXCO_2 calculated from CT2015, together with full column
353 ΔXCO_2 from individual aircraft sites (note that some aircraft sites have less than 11 years of data the CT2015 shows
354 in Fig. 9, only aircraft sites with more than 6 years of data are presented). The fact that total column ΔXCO_2 from
355 CT2015 agrees well with aircraft sites also supports the performance of CT2015 on a long-term average basis. The
356 observations show a similar summer spatial pattern, with lower column ΔXCO_2 in the north and northeast regions
357 and higher column ΔXCO_2 in the south and southwest regions (Fig. 9a). Scattered hot spots of high column ΔXCO_2
358 associated with surface emissions from megacities, or cold spots associated with strong local uptake, are not or just
359 barely visible in the long-term average column ΔXCO_2 map at $1^\circ \times 1^\circ$ resolution. Instead, the wave-like pattern of
360 column ΔXCO_2 over North America reflects large scale circulation. To support our hypothesis on the influence of
361 large scale circulation, we analyze the long term mean wind pattern over North America. We can see that air masses
362 from northwest of the continent bring in low average column ΔXCO_2 , while air masses from the south (mainly the
363 subtropical Pacific Ocean and the Gulf of Mexico) bring in high column ΔXCO_2 (Fig. 9b). The zonal gradients over
364 the continent, especially north of $40^\circ N$, also reflect long-term average wind patterns; southwest wind corresponds to
365 higher column ΔXCO_2 over the western part of the continent until the wind direction shifts to west-northwest over

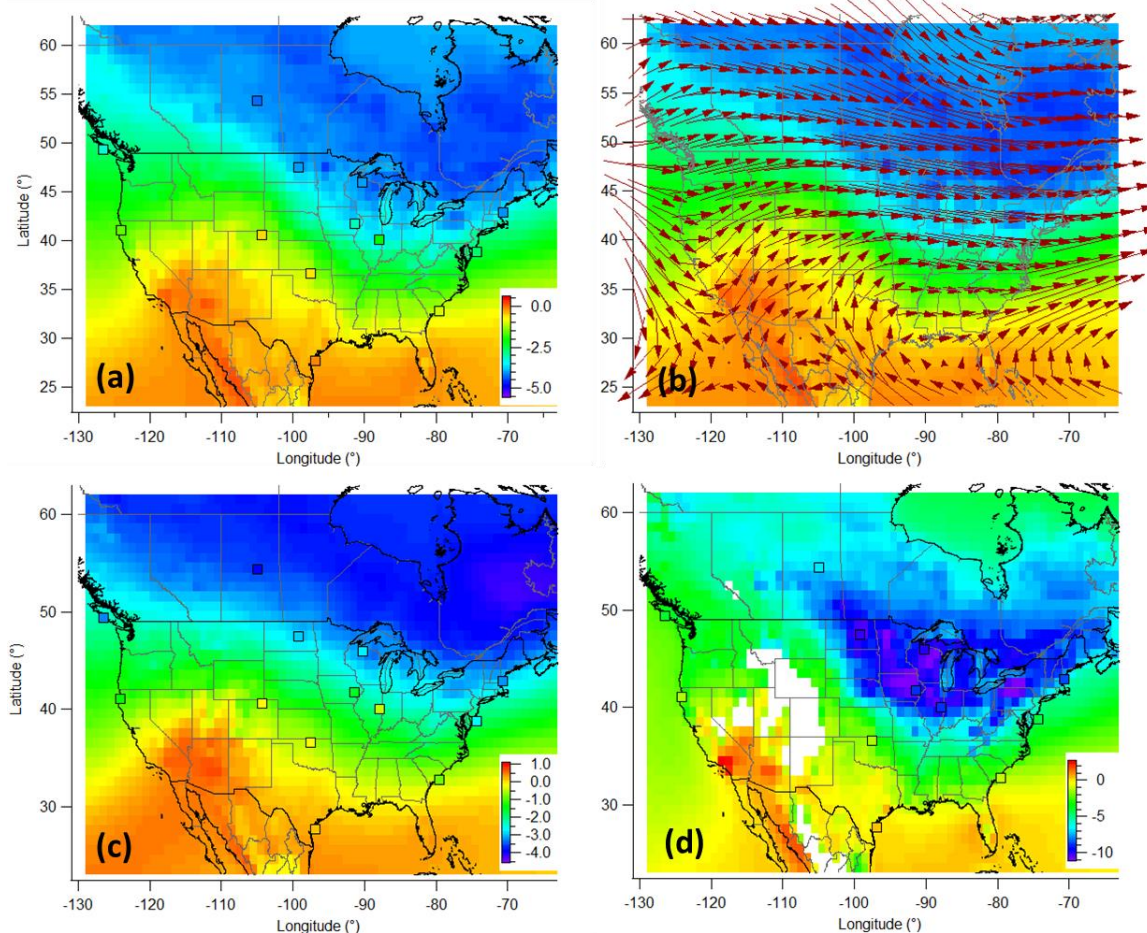


366 the eastern part of the continent. This wind pattern matches well with the geographic division of the over/under -3
367 ppm areas colored in green/blue in the column ΔXCO_2 map (Fig. 9b). Figure 9c and 9d shows partial column
368 averages for free troposphere (800-330 hPa) and lower troposphere (below 800 hPa), respectively. The free
369 troposphere spatial gradient also demonstrates a wave-like pattern. A previous study on the total column CO_2 from
370 ground based Total Carbon Column Observation Network (TCCON) found strong correlation between the mid-
371 latitude column CO_2 and synoptic-scale variation of potential temperature (θ , at 700 hPa), a dynamic tracer for
372 adiabatic air transport (Keppel-Aleks et al., 2012). Thus they also propose that the variations in column CO_2 are
373 mainly driven by large-scale flux and transport.

374 The strong drawdown over northeast North America in summer is a consequence of long-range transport of low
375 CO_2 from northeast Eurasia, in addition to regional terrestrial uptake. Sweeney et al. (2015) notes well-mixed
376 vertical profiles (up to 8 km) of CO_2 , CO, CH_4 , N_2O , and SF_6 from THD, ESP and PFA (Poker Flat, Alaska; 65.07°,
377 -147.29°) sites and suggests that air coming across the Pacific was strongly influenced by Asian surface fluxes
378 before being vertically homogenized as it passed over the Pacific Ocean. This well-mixed air forms an important
379 boundary condition in the column CO_2 of air coming into the North American continent. This was best illustrated at
380 sites like PFA where the summertime minimum in CO_2 significantly preceded maximum ecosystem uptake of CO_2 ,
381 implying significant influence of transported air from lower latitude regions from Asia. We further conduct an
382 experiment using Carbon Tracker to investigate the importance of this effect. A control run and a “masked run” are
383 conducted for 2010-2012, in which the Eurasian boreal flux is turned on/off. The MLO CO_2 trend from each model
384 scenario is used as reference background and thus removed before total column ΔXCO_2 calculation. Figure 10 shows
385 the results for 2012 summer, which is an average summer when compared with the 2004-2014 mean pattern (Fig. 9
386 and Fig. 11). The maximum north-south difference reduces to ~2.5 ppm after we turn off the Eurasian boreal flux,
387 compared with ~5 ppm from the control run. This result combined with results from Sweeney et al. (2015)
388 demonstrates that the transport of low CO_2 resulting from large summertime Eurasian boreal uptake has a large
389 contribution on the overall summer total column CO_2 drawdown in North America.

390

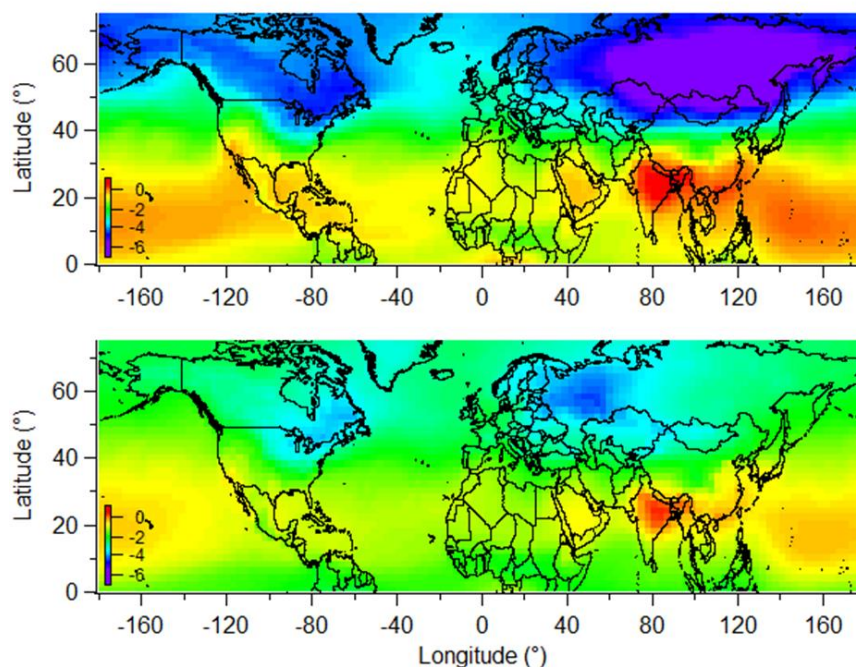
391



392

393 **Fig. 9.** Long-term mean (2004-2014) June-August total column ΔXCO_2 from CT2015 in $1^\circ \times 1^\circ$ spatial resolution
394 with total column ΔXCO_2 for 13 individual aircraft sites in squares (a), and CT2015 column ΔXCO_2 overlaid with
395 pressure-weighted (1000 hPa to 500 hPa) mean wind vectors for the same period (b). (c) and (d) are similar as (a),
396 except for free troposphere (800 to 330 hPa) and lower troposphere (below 800 hPa), respectively. Note the different
397 color scales.

398



399

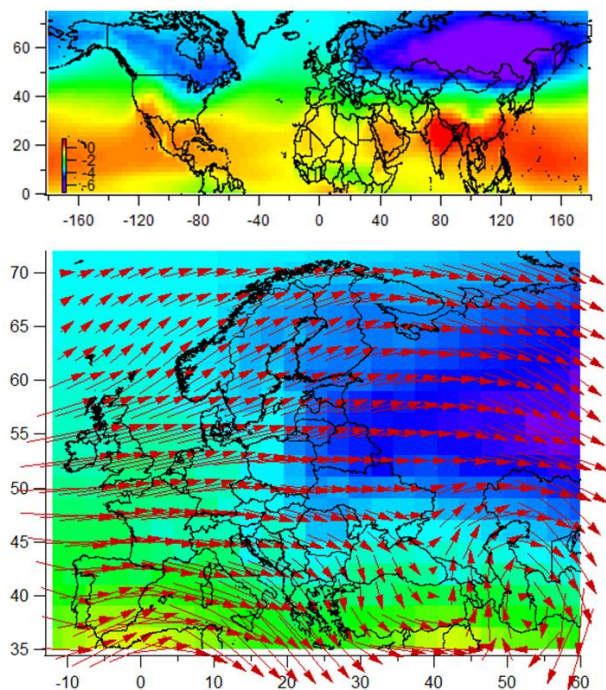
400 **Fig. 10.** Total column ΔXCO_2 from Carbon Tracker control (top panel) and masked (bottom panel, Eurasian boreal
401 flux is masked) runs for 2012 June-August ($3^\circ \times 2^\circ$ spatial resolution). MLO trend from each individual scenario is
402 removed before the ΔXCO_2 calculation. Same color scale is used as in Fig. 9a.

403 3.5 A comparison with apparent gradients over Europe

404 Figure 11 shows the climatological June - August mean modeled global column ΔXCO_2 map in $3^\circ \times 2^\circ$ spatial
405 resolution, which presents smooth wave-like patterns. Reuter et al. (2014) use SCIAMACHY and GOSAT satellite
406 retrievals of column CO_2 and inverse modelling to attain surface CO_2 flux over European region, and suggest a large
407 uptake of CO_2 in this region. Column ΔXCO_2 from CT2015 (Fig. 11) exhibits a drastically different summer spatial
408 pattern over Europe compared with the eight year mean (2003-2010) June through August satellite retrievals
409 presented by Reuter et al. (2014, their Fig. 2a). The spatial gradient from CT2015 results in a maximum 3-4 ppm
410 difference and a gradual pattern, instead of as much as 6 ppm from satellite retrievals. There is no sign of XCO_2 hot
411 spots from surface emissions or removals in the CT2015 spatial pattern over Europe (Fig. 11), in contrast to several
412 hot spots that are apparent from the 8-year averaged SCIAMACHY satellite retrievals over Ireland, U.K., northeast
413 of France, Belgium, Netherland, north of Germany, and south of Sweden, and low spots over the Ukraine and
414 Kazakhstan (Reuter et al., 2014). Although the NOAA/ESRL CT2015
415 (<https://www.esrl.noaa.gov/gmd/ccgg/carbontracker/CT2015/>) assimilates fewer observations over Europe than
416 Carbon Tracker Europe (<http://www.carbontracker.eu/>), both models produced similar fluxes over the European
417 region (see both websites for detailed fluxes). The $3^\circ \times 2^\circ$ grid from CT2015 is not likely responsible for a much



418 smoother pattern for Carbon Tracker, compared with the $2^\circ \times 2^\circ$ grid from satellite retrievals (Reuter et al., 2014) .
419 The North America region on the $3^\circ \times 2^\circ$ grid in Fig. 11 shows similar pattern as the $1^\circ \times 1^\circ$ grid in Fig. 9, with
420 similar spatial difference of ~ 5 ppm. A smoother spatial distribution should be expected in Europe for the long-term
421 mean column XCO_2 (Fig. 11) due to the influences of dominating west and southwest winds in summer. Since the
422 satellite retrievals in Reuter et al. (2014) appear to show unrealistic column XCO_2 spatial gradients over Europe,
423 they should not be used to derive estimates of a European carbon sink. A recent study (Feng et al., 2016) using
424 inverse modeling suggests that satellite retrievals outside the immediate European region and a small bias of 0.5
425 ppm were sufficient to produce the apparent large carbon sink in the study of Reuter et al. (2014). This is expected
426 from elementary mass balance considerations as in Sec.1. Spatial gradients are the fundamental signals to infer
427 regional fluxes. Since spatial gradients from CT2015 are realistic, boreal fluxes inferred by CT2015, which shows
428 0.03 ± 2.33 Pg C yr⁻¹ for Europe, should be more trustworthy.
429
430



431
432 **Fig. 11.** Long-term mean (2004-2014) June - August total column ΔXCO_2 from CT2015 (top panel) in $3^\circ \times 2^\circ$
433 spatial resolution, and zoom-in for Europe overlaid with pressure-weighted (1000 hPa to 500 hPa) mean wind
434 vectors for the same period (bottom panel). The color scale is the same as in Fig. 9a, which is scaled to reflect 6
435 ppm difference of XCO_2 to compare with satellite retrievals from Reuter et al. (their Fig. 2a, 2014).



436 **4 Conclusion**

437 Aircraft and tall tower measurements from the NOAA GGGRN provide detailed information describing the long-
438 term average temporal and spatial variations of CO₂ in the PBL and the free troposphere. These data provide
439 valuable constraints for evaluating model simulations and satellite retrievals. Seasonal cycle peak-to-peak
440 amplitudes of CO₂ are largest below 2 km, where those maximum values are about twice those in the vertical layers
441 above, indicating that most of the information on surface sources and sinks resides in the continental PBL. Large
442 spatial gradients of CO₂ over North America are observed below 2 km during summer, while higher altitude data
443 (above 2 km) have much smaller contributions to spatial gradients, with a maximum difference of only 4 ppm. The
444 spatial differences of CO₂ in the upper troposphere and above (330 hPa to 0 hPa) are less than 0.5 ppm, according
445 to CT2015. Comparison with Aircore measurements shows that the upper troposphere and lower stratospheric
446 simulations from CT2015 are reasonably trustworthy.

447 Our long-term mean vertical profiles show that tower data agree well with aircraft data at similar vertical levels.
448 Partial column ΔXCO_2 was calculated from the long-term mean vertical profiles. By comparing the partial column
449 ΔXCO_2 from measurements with those from CT2015, we verify that CT2015 captures the long-term mean patterns
450 of both phase and amplitude of partial ΔXCO_2 .

451 Large spatial gradients of ΔXCO_2 only appeared in summer, during which time the north and northeast regions
452 had ~3 ppm stronger drawdowns than the south and southwest regions. By comparing the spatial gradients of
453 ΔXCO_2 with wind vectors across North America, we find that total column ΔXCO_2 patterns are equally affected by
454 large-scale circulation patterns as by regional surface sources and sinks. A CarbonTracker experiment to investigate
455 the impact of Eurasian long-range transport suggests that the large summer time Eurasian boreal flux contributes
456 about half of the north-south column ΔXCO_2 gradient across North America.

457 **Author contributions**

458 Xin Lan was responsible for study design, data analysis, and manuscript writing. Pieter Tans was responsible for
459 study design, data analysis, and manuscript improvement. Colm Sweeney and Arlyn Andrews provided
460 measurement data and improved manuscript. Andrew Jacobson provided modelled data and improved manuscript.
461 Edward Dlugokencky analyzed measurements and ensured data quality, and improved manuscript. Jonathan Kofler
462 conducted tower measurements and improved manuscript. Molly Crotwell, Patricia Lang, and Sonja Wolter
463 analyzed measurements and ensured data quality. Kirk Thoning provided data smoothing method.

464 **Acknowledgements**

465 We especially thank John Mund for extracting NARR meteorological variables for our measurements. This
466 research was supported by a fellowship from the National Research Council Research Associateship Programs.

467 **References**

- 468 Andrews, A. E., Kofler, J. D., Trudeau, M. E., Williams, J. C., Neff, D. H., Masarie, K. A., Chao, D. Y., Kitzis, D.
469 R., Novelli, P. C., Zhao, C. L., Dlugokencky, E. J., Lang, P. M., Crotwell, M. J., Fischer, M. L., Parker, M. J.,
470 Lee, J. T., Baumann, D. D., Desai, A. R., Stanier, C. O., De Wekker, S. F. J., Wolfe, D. E., Munger, J. W. and
471 Tans, P. P.: CO₂, CO, and CH₄ measurements from tall towers in the NOAA Earth System Research
472 Laboratory's Global Greenhouse Gas Reference Network: instrumentation, uncertainty analysis, and
473 recommendations for future high-accuracy greenhouse gas monitoring efforts, *Atmos. Meas. Tech.*, 7, 647-687,
474 2014.
- 475 Banta, R. M., Senff, C. J., Nielsen-Gammon, J., Darby, L. S., Ryerson, T. B., Alvarez, R. J., Sandberg, S. R.,
476 Williams, E. J. and Trainer, M.: A bad air day in Houston', *B. Am. Meteorol. Soc.*, 86, 657, DOI:
477 <http://dx.doi.org/10.1175/BAMS-86-5-657>, 2005.
- 478 Biraud, S. C., Torn, M. S., Smith, J. R., Sweeney, C., Riley, W. J. and Tans, P. P.: A multi-year record of airborne
479 CO₂ observations in the US Southern Great Plains, *Atmos. Meas. Tech.*, 6, 751-763, 2013.
- 480 Buchwitz, M., Reuter, M., Bovensmann, H., Pillai, D., Heymann, J., Schneising, O., Rozanov, V., Krings, T.,
481 Burrows, J. P., Boesch, H., Gerbig, C., Meijer, Y. and Loscher, A. : Carbon Monitoring Satellite (CarbonSat):
482 assessment of atmospheric CO₂ and CH₄ retrieval errors by error parameterization, *Atmos. Meas. Tech.*, 6,
483 3477-3500, 2013.
- 484 Chevallier, F., Breon, F. M. and Rayner, P. J.: Contribution of the Orbiting Carbon Observatory to the estimation of
485 CO₂ sources and sinks: Theoretical study in a variational data assimilation framework, *J. Geophys. Res.*
486 *Atmos.*, 112, D09307, doi:10.1029/2006JD007375, 2007.
- 487 Choi, Y. H., Vay, S. A., Vadrevu, K. P., Soja, A. J., Woo, J. H., Nolf, S. R., Sachse, G. W., Diskin, G. S., Blake, D.
488 R., Blake, N. J., Singh, H. B., Avery, M. A., Fried, A., Pfister, L. and Fuelberg, H. E.: Characteristics of the
489 atmospheric CO₂ signal as observed over the conterminous United States during INTEX-NA, *J. Geophys. Res.*
490 *Atmos.*, 113, D07301, doi:10.1029/2007JD008899, 2008.
- 491 Ciais, P., Rayner, P., Chevallier, F., Bousquet, P., Logan, M., Peylin, P. and Ramonet, M.: Atmospheric inversions
492 for estimating CO₂ fluxes: methods and perspectives, *Climatic Change*, 103, 69-92, 2010.
- 493 Conway, T. J., Tans, P. P., Waterman, L. S. and Thoning, K. W.: Evidence for interannual variability of the carbon-
494 cycle from the national-oceanic-and-atmospheric-administration climate-monitoring-and-diagnostics-laboratory
495 global-air-sampling-network, *J. Geophys. Res. Atmos.*, 99, 22831-22855, 1994.
- 496 Crevoisier, C., Sweeney, C., Gloor, M., Sarmiento, J. L. and Tans, P. P.: Regional US carbon sinks from three-
497 dimensional atmospheric CO₂ sampling, *Proc. Natl. Acad. Sci. U. S. A.*, 107, 18348-18353, 2010.
- 498 Crisp, D., Fisher, B. M., O'Dell, C., Frankenberg, C., Basilio, R., Bosch, H., Brown, L. R., Castano, R., Connor, B.,
499 Deutscher, N. M., Eldering, A., Griffith, D., Gunson, M., Kuze, A., Mandrake, L., McDuffie, J.,
500 Messerschmidt, J., Miller, C. E., Morino, I., Natraj, V., Notholt, J., O'Brien, D. M., Oyafuso, F., Polonsky, I.,
501 Robinson, J., Salawitch, R., Sherlock, V., Smyth, M., Suto, H., Taylor, T. E., Thompson, D. R., Wennberg, P.
502 O., Wunch, D., and Yung, Y. L.: The ACOS CO₂ retrieval algorithm – Part II: Global XCO₂ data
503 characterization, *Atmos. Meas. Tech.*, 5, 687–707, doi:10.5194/amt-5-687-2012, 2012.



- 504 Dee, D. P., Uppala, S. M., Simmons, A. J., Berrisford, P., Poli, P., Kobayashi, S., Andrae, U., Balmaseda, M. A.,
505 Balsamo, G., Bauer, P., Bechtold, P., Beljaars, A. C. M., van de Berg, L., Bidlot, J., Bormann, N., Delsol, C.,
506 Dragani, R., Fuentes, M., Geer, A. J., Haimberger, L., Healy, S. B., Hersbach, H., Holm, E. V., Isaksen, L.,
507 Kallberg, P., Kohler, M., Matricardi, M., McNally, A. P., Monge-Sanz, B. M., Morcrette, J. J., Park, B. K.,
508 Peubey, C., de Rosnay, P., Tavolato, C., Thepaut, J. N. and Vitart, F.: The ERA-Interim reanalysis:
509 configuration and performance of the data assimilation system, *Q.J.R. Meteorol. Soc.*, 137, 553-597, 2011.
- 510 Denning, A. S., Takahashi, T., and Friedlingstein, P.: Can a strong atmospheric CO₂ rectifier effect be reconciled
511 with a “reasonable” carbon budget?, *Tellus B*, 51, 249–253, 1999.
- 512 Feng, L., Palmer, P. I., Parker, R. J., Deutscher, N. M., Feist, D. G., Kivi, R., Morino, I. and Sussmann, R.:
513 Estimates of European uptake of CO₂ inferred from GOSAT X-CO₂ retrievals: sensitivity to measurement bias
514 inside and outside Europe, *Atmos. Chem. Phys.*, 16, 1289-1302, 2016.
- 515 Frankenberg, C., Kulawik, S. S., Wofsy, S., Chevallier, F., Daube, B., Kort, E. A., O'Dell, C., Olsen, E. T., and
516 Osterman, G.: Using airborne HIAPER Pole-to-Pole Observations (HIPPO) to evaluate model and remote
517 sensing estimates of atmospheric carbon dioxide, *Atmos. Chem. Phys.*, 16, 7867–7878, 2016. doi:10.5194/acp-
518 16-7867-2016, 2016.
- 519 Gerbig, C., Lin, J. C., Wofsy, S. C., Daube, B. C., Andrews, A. E., Stephens, B. B., Bakwin, P. S. and Grainger, C.
520 A.: Toward constraining regional-scale fluxes of CO₂ with atmospheric observations over a continent: 1.
521 Observed spatial variability from airborne platforms *J. Geophys. Res. Atmos.*, 108, doi:10.1029/2002JD003018,
522 2003.
- 523 Gourdji, S. M., Mueller, K. L., Yadav, V., Huntzinger, D. N., Andrews, A. E., Trudeau, M., Petron, G., Nehr Korn,
524 T., Eluszkiewicz, J., Henderson, J., Wen, D., Lin, J., Fischer, M., Sweeney, C. and Michalak, A. M.: North
525 American CO₂ exchange: inter-comparison of modeled estimates with results from a fine-scale atmospheric
526 inversion, *Biogeosci.*, 9, 457-475, 2012
- 527 Gurney, K. R., Law, R. M., Denning, A. S., Rayner, P. J., Baker, D., Bousquet, P., Bruhwiler, L., Chen, Y. H., Ciais,
528 P., Fan, S., Fung, I. Y., Gloor, M., Heimann, M., Higuchi, K., John, J., Maki, T., Maksyutov, S., Masarie, K.,
529 Peylin, P., Prather, M., Pak, B. C., Randerson, J., Sarmiento, J., Taguchi, S., Takahashi, T. and Yuen, C. W.:
530 Towards robust regional estimates of CO₂ sources and sinks using atmospheric transport models, *Nature*,
531 415(6872), 626-630, 2002.
- 532 Gurney, K. R., Law, R. M., Denning, A. S., Rayner, P. J., Pak, B. C., Baker, D., Bousquet, P., Bruhwiler, L., Chen,
533 Y. H., Ciais, P., Fung, I. Y., Heimann, M., John, J., Maki, T., Maksyutov, S., Peylin, P., Prather, M. and
534 Taguchi, S.: Transcom 3 inversion intercomparison: Model mean results for the estimation of seasonal carbon
535 sources and sinks, *Global Biogeochem. Cycles*, 18, GB1010, doi:10.1029/2003GB002111, 2004.
- 536 Houweling, S., Breon, F. M., Aben, I., Rodenbeck, C., Gloor, M., Heimann, M. and Ciais, P.: Inverse modeling of
537 CO₂ sources and sinks using satellite data: a synthetic inter-comparison of measurement techniques and their
538 performance as a function of space and time, *Atmos. Chem. Phys.*, 4, 523-538, 2004.
- 539 Inoue, M., Morino, I., Uchino, O., Miyamoto, Y., Yoshida, Y., Yokota, T., Machida, T., Sawa, Y., Matsueda, H.,
540 Sweeney, C., Tans, P. P., Andrews, A. E., Biraud, S. C., Tanaka, T., Kawakami, S. and Patra, P. K.: Validation



- 541 of XCO₂ derived from SWIR spectra of GOSAT TANSO-FTS with aircraft measurement data, *Atmos. Chem.*
542 *Phys.*, 13, 9771-9788, 2013.
- 543 Inoue, M., Morino, I., Uchino, O., Nakatsuru, T., Yoshida, Y., Yokota, T., Wunch, D., Wennberg, P. O., Roehl, C.
544 M., Griffith, D. W. T., Velazco, V. A., Deutscher, N. M., Warneke, T., Notholt, J., Robinson, J., Sherlock, V.,
545 Hase, F., Blumenstock, T., Rettinger, M., Sussmann, R., Kyrö, E., Kivi, R., Shiomi, K., Kawakami, S., De
546 Mazière, M., Arnold, S. G., Feist, D. G., Barrow, E. A., Barney, J., Dubey, M., Schneider, M., Iraci, L.,
547 Podolske, J. R., Hillyard, P., Machida, T., Sawa, Y., Tsuboi, K., Matsueda, H., Sweeney, C., Tans, P. P.,
548 Andrews, A. E., Biraud, S. C., Fukuyama, Y., Pittman, J. V., Kort, E. A., and Tanaka, T.: Bias corrections of
549 GOSAT SWIR XCO₂ and XCH₄ with TCCON data and their evaluation using aircraft measurement data,
550 *Atmos. Meas. Tech.* 9, 3491–3512, 2016, doi:10.5194/amt-9-3491-2016.
- 551 Karion, A., Sweeney, C., Tans, P., and Newberger, T.: AirCore: An Innovative Atmospheric Sampling System, *J.*
552 *Atmos. Ocean. Tech.*, 27, 1839–1853, doi:10.1175/2010JTECHA1448.1, 2010.
- 553 Karion, A., C. Sweeney, S. Wolter, T. Newberger, H. Chen, A. Andrews, J. Kofler, D. Neff, and P. Tans (2013),
554 Long-term greenhouse gas measurements from aircraft, *Atmos. Meas. Tech.*, 6(3), 511–526, doi:10.5194/amt-6-
555 511-2013.
- 556 Keeling, C. D. and Rakestraw, N. W.: The concentration of carbon dioxide in the atmosphere, *J. Geophys. Res.*, 65,
557 2502-2502, 1960.
- 558 Keppel-Aleks, G., Wennberg, P. O., Washenfelder, R. A., Wunch, D., Schneider, T., Toon, G. C., Andres, R. J.,
559 Blavier, J.-F., Connor, B., Davis, K. J., Desai, A. R., Messerschmidt, J., Notholt, J., Roehl, C. M., Sherlock, V.,
560 Stephens, B. B., Vay, S. A., and Wofsy, S. C.: The imprint of surface fluxes and transport on variations in total
561 column carbon dioxide, *Biogeosci.*, 9, 875–891, doi:10.5194/bg-9-875-2012, 2012.
- 562 Kulawik, S. S., Worden, J. R., Wofsy, S. C., Biraud, S. C., Nassar, R., Jones, D. B. A., Olsen, E. T., Jimenez, R.,
563 Park, S., Santoni, G. W., Daube, B. C., Pittman, J. V., Stephens, B. B., Kort, E. A., Osterman, G. B. and Team,
564 T. E. S.: Comparison of improved Aura Tropospheric Emission Spectrometer CO₂ with HIPPO and SGP
565 aircraft profile measurements, *Atmos. Chem. Phys.*, 13, 3205-3225, 2013.
- 566 Lauvaux, T., Schuh, A. E., Uliasz, M., Richardson, S., Miles, N., Andrews, A. E., Sweeney, C., Diaz, L. I., Martins,
567 D., Shepson, P. B. and Davis, K. J.: Constraining the CO₂ budget of the corn belt: exploring uncertainties from
568 the assumptions in a mesoscale inverse system, *Atmos. Chem. Phys.*, 12, 337-354, 2012.
- 569 Machida, T., Kita, K., Kondo, Y., Blake, D., Kawakami, S., Inoue, G. and Ogawa, T. : Vertical and meridional
570 distributions of the atmospheric CO₂ mixing ratio between northern midlatitudes and southern subtropics, *J.*
571 *Geophys. Res. Atmos.*, 108(D3), 8401, doi:10.1029/2001JD000910, 2002.
- 572 Machida, T., Matsueda, H., Sawa, Y., Nakagawa, Y., Hirotsu, K., Kondo, N., Goto, K., Nakazawa, T., Ishikawa, K.
573 and Ogawa, T.: Worldwide Measurements of Atmospheric CO₂ and Other Trace Gas Species Using
574 Commercial Airlines, *J. Atmos. Ocean. Tech.*, 25(10), 1744-1754, 2008.
- 575 Mesinger, F., DiMego, G., Kalnay, E., Mitchell, K., Shafran, P. C., Ebisuzaki, W., Jovic, D., Woollen, J., Rogers,
576 E., Berbery, E. H., Ek, M. B., Fan, Y., Grumbine, R., Higgins, W., Li, H., Lin, Y., Manikin, G., Parrish, D., and



- 577 Shi, W.: North American regional reanalysis, *B. Am. Meteorol. Soc.*, 87, 343–360, doi:10.1175/BAMS-87-3-
578 343, 2006.
- 579 Messerschmidt, J., Geibel, M. C., Blumenstock, T., Chen, H., Deutscher, N. M., Engel, A., Feist, D. G., Gerbig, C.,
580 Gisi, M., Hase, F., Katrynski, K., Kolle, O., Lavric, J. V., Notholt, J., Palm, M., Ramonet, M., Rettinger, M.,
581 Schmidt, M., Sussmann, R., Toon, G. C., Truong, F., Warneke, T., Wennberg, P. O., Wunch, D. and Xueref-
582 Remy, I.: Calibration of TCCON column-averaged CO₂: the first aircraft campaign over European TCCON
583 sites, *Atmos. Chem. Phys.*, 11(21), 10765-10777, 2011.
- 584 Miller, C. E., Crisp, D., DeCola, P. L., Olsen, S. C., Randerson, J. T., Michalak, A. M., Alkhaled, A., Rayner, P.,
585 Jacob, D. J., Suntharalingam, P., Jones, D. B. A., Denning, A. S., Nicholls, M. E., Doney, S. C., Pawson, S.,
586 Boesch, H., Connor, B. J., Fung, I. Y., O'Brien, D., Salawitch, R. J., Sander, S. P., Sen, B., Tans, P., Toon, G.
587 C., Wennberg, P. O., Wofsy, S. C., Yung, Y. L. and Law, R. M.: Precision requirements for space-based X-CO₂
588 data, *J. Geophys. Res. Atmos.*, 112, D10314, doi:10.1029/2006JD007659, 2007.
- 589 Miller, J. B., Lehman, S. J., Montzka, S. A., Sweeney, C., Miller, B. R., Karion, A., Wolak, C., Dlugokencky, J.,
590 Southon, J., Turnbull, J. C., and Tans, P. P.: Linking emissions of fossil fuel CO₂ and other anthropogenic trace
591 gases using atmospheric ¹⁴CO₂, *J. Geophys. Res.*, 117, D08302, doi:10.1029/2011JD017048, 2012.
- 592 Miller, S. T. K., Keim, B. D., Talbot, R. W. and Mao, H.: Sea breeze: Structure, forecasting, and impacts, *Rev.*
593 *Geophys.*, 41, 1011, doi:10.1029/2003RG000124, 2003.
- 594 Miyamoto, Y., Inoue, M., Morino, I., Uchino, O., Yokota, T., Machida, T., Sawa, Y., Matsueda, H., Sweeney, C.,
595 Tans, P. P., Andrews, A. E. and Patra, P. K.: Atmospheric column-averaged mole fractions of carbon dioxide at
596 53 aircraft measurement sites, *Atmos. Chem. Phys.*, 13(10), 5265-5275, 2013.
- 597 Peters, W., Jacobson, A. R., Sweeney, C., Andrews, A. E., Conway, T. J., Masarie, K., Miller, J. B., Bruhwiler, L.
598 M. P., Petron, G., Hirsch, A. I., Worthy, D. E. J., van der Werf, G. R., Randerson, J. T., Wennberg, P. O., Krol,
599 M. C. and Tans, P. P.: An atmospheric perspective on North American carbon dioxide exchange:
600 CarbonTracker, *Proc. Natl. Acad. Sci. U. S. A.*, 104(48), 18925-18930, 2007.
- 601 Ramonet, M., Ciais, P., Nepomniachii, I., Sidorov, K., Neubert, R. E. M., Langendorfer, U., Picard, D., Kazan, V.,
602 Biraud, S., Gusti, M., Kolle, O., Schulze, E. D. and Lloyd, J.: Three years of aircraft-based trace gas
603 measurements over the Fyodorovskoye southern taiga forest, 300 km north-west of Moscow, *Tellus B-Chem.*
604 *Phys. Meteor.*, 54(5), 713-734, 2002.
- 605 Reuter, M., Bovensmann, H., Buchwitz, M., Burrows, J. P., Connor, B. J., Deutscher, N. M., Griffith, D. W. T.,
606 Heymann, J., Keppel-Aleks, G., Messerschmidt, J., Notholt, J., Petri, C., Robinson, J., Schneising, O., Sherlock,
607 V., Velasco, V., Warneke, T., Wennberg, P. O. and Wunch, D.: Retrieval of atmospheric CO₂ with enhanced
608 accuracy and precision from SCIAMACHY: Validation with FTS measurements and comparison with model
609 results, *J. Geophys. Res. Atmos.*, 116, 2011.
- 610 Reuter, M., Buchwitz, M., Hilker, M., Heymann, J., Schneising, O., Pillai, D., Bovensmann, H., Burrows, J. P.,
611 Bosch, H., Parker, R., Butz, A., Hasekamp, O., O'Dell, C. W., Yoshida, Y., Gerbig, C., Nehr Korn, T.,
612 Deutscher, N. M., Warneke, T., Notholt, J., Hase, F., Kivi, R., Sussmann, R., Machida, T., Matsueda, H. and



- 613 Sawa, Y.: Satellite-inferred European carbon sink larger than expected, *Atmos. Chem. Phys.*, 14(24), 13739-
614 13753, 2014.
- 615 Saitoh, N., Kimoto, S., Sugimura, R., Imasu, R., Kawakami, S., Shiomi, K., Kuze, A., Machida, T., Sawa, Y. and
616 Matsueda, H.: Algorithm update of the GOSAT/TANSO-FTS thermal infrared CO₂ product (version 1) and
617 validation of the UTLS CO₂ data using CONTRAIL measurements, *Atmos. Meas. Tech.*, 9(5), 2119-2134,
618 2016.
- 619 Stephens, B. B., Gurney, K. R., Tans, P. P., Sweeney, C., Peters, W., Bruhwiler, L., Ciais, P., Ramonet, M.,
620 Bousquet, P., Nakazawa, T., Aoki, S., Machida, T., Inoue, G., Vinnichenko, N., Lloyd, J., Jordan, A., Heimann,
621 M., Shibistova, O., Langenfelds, R. L., Steele, L. P., Francey, R. J. and Denning, A. S.: Weak northern and
622 strong tropical land carbon uptake from vertical profiles of atmospheric CO₂, *Science*, 316(5832), 1732-1735,
623 2007.
- 624 Sweeney, C., Karion, A., Wolter, S., Newberger, T., Guenther, D., Higgs, J. A., Andrews, A. E., Lang, P. M., Neff,
625 D., Dlugokencky, E., Miller, J. B., Montzka, S. A., Miller, B. R., Masarie, K. A., Biraud, S. C., Novelli, P. C.,
626 Crotnell, M., Crotnell, A. M., Thoning, K. and Tans, P. P.: Seasonal climatology of CO₂ across North America
627 from aircraft measurements in the NOAA/ESRL Global Greenhouse Gas Reference Network, *J. Geophys. Res.*
628 *Atmos.*, 120(10), 5155-5190, 2015.
- 629 Tanaka, M., Nakazawa, T. and Aoki, S.: Concentration of atmospheric carbon-dioxide over Japan, *J. Geophys. Res.*
630 *Ocean.*, 88(C2), 1339-1344, DOI: 10.1029/JC088iC02p01339, 1983.
- 631 Tanaka, T., Miyamoto, Y., Morino, I., Machida, T., Nagahama, T., Sawa, Y., Matsueda, H., Wunch, D., Kawakami,
632 S. and Uchino, O.: Aircraft measurements of carbon dioxide and methane for the calibration of ground-based
633 high-resolution Fourier Transform Spectrometers and a comparison to GOSAT data measured over Tsukuba
634 and Moshiri, *Atmos. Meas. Tech.*, 5(8), 2003-2012, 2012.
- 635 Tans, P. P., Conway, T. J. and Nakazawa, T.: Latitudinal distribution of the sources and sinks of atmospheric
636 carbon-dioxide derived from surface observations and an atmospheric transport model, *J. Geophys. Res.*
637 *Atmos.*, 94(D4), 5151-5172, 1989.
- 638 Tans, P. P., Fung, I. Y. and Takahashi, T.: Observational constraints on the global atmospheric CO₂ budget, *Science*,
639 247(4949), 1431-1438, 1990.
- 640 Thoning, K. W., Tans, P. P. and Komhyr, W. D.: Atmospheric carbon-dioxide at Mauna Loa observatory. 2.
641 Analysis of the NOAA GMCC data, 1974-1985, *J. Geophys. Res. Atmos.*, 94(D6), 8549-8565, 1989.
- 642 Washenfelder, R. A., Toon, G. C., Blavier, J. F., Yang, Z., Allen, N. T., Wennberg, P. O., Vay, S. A., Matross, D.
643 M. and Daube, B. C.: Carbon dioxide column abundances at the Wisconsin Tall Tower site, *J. Geophys. Res.*
644 *Atmos.*, 111, D22305, doi:10.1029/2006JD007154, 2006.
- 645 Wofsy, S. C.: HIPPER Pole-to-Pole Observations (HIPPO): finegrained, global-scale measurements of climatically
646 important atmospheric gases and aerosols, *Philos. T. R. Soc. A*, 369, 2073-2086, doi:10.1098/rsta.2010.0313,
647 2011.
- 648 Wunch, D., Toon, G. C., Wennberg, P. O., Wofsy, S. C., Stephens, B. B., Fischer, M. L., Uchino, O., Abshire, J. B.,
649 Bernath, P., Biraud, S. C., Blavier, J. F. L., Boone, C., Bowman, K. P., Browell, E. V., Campos, T., Connor, B.



650 J., Daube, B. C., Deutscher, N. M., Diao, M., Elkins, J. W., Gerbig, C., Gottlieb, E., Griffith, D. W. T., Hurst,
651 D. F., Jimenez, R., Keppel-Aleks, G., Kort, E. A., Macatangay, R., Machida, T., Matsueda, H., Moore, F.,
652 Morino, I., Park, S., Robinson, J., Roehl, C. M., Sawa, Y., Sherlock, V., Sweeney, C., Tanaka, T. and Zondlo,
653 M. A.: Calibration of the Total Carbon Column Observing Network using aircraft profile data', Atmos. Meas.
654 Tech., 3(5), 1351-1362, 2010.